Journal of Alloys and Compounds 937 (2023) 168379

Contents lists available at ScienceDirect

Journal of Alloys and Compounds

journal homepage: www.elsevier.com/locate/jalcom

NiS_2 nanospheres coated by nitrogen-doped carbon for enhanced sodium storage performance

W.X. Zhang [a], J.H. Zhang [a], J.Q. Guo [a], C. He [b,*], J.R. Wen [a,*]

[a] School of Materials Science and Engineering, Chang'an University, Xi'an 710064, China
[b] State Key Laboratory for Mechanical Behavior of Materials, School of Materials Science and Engineering, Xi'an Jiaotong University, Xi'an 710049, China

ARTICLE INFO

Article history:
Received 18 September 2022
Received in revised form 23 November 2022
Accepted 4 December 2022
Available online 5 December 2022

Keywords:
NiS_2@NC
PVP-assisted hydrothermal
Charge storage mechanism
Sodium-ion battery

ABSTRACT

Nickel disulfide is used as anode material for sodium-ion batteries, with low cost, abundant reserves, and a wide variety of theoretical specific capacities as high as 870 mAh g^{-1}. However, large volume expansion and low ionic conductivity during Na^+ intercalation and deintercalation lead to poor electrochemical performance. This work has synthesized carbon layer-coated and N-doped NiS_2 nanospheres through PVP-assisted hydrothermal and subsequent annealing processes, reducing volume expansion and improving electrical conductivity and Na^+ storage activity, increasing ion diffusion kinetics during electrochemical charge-discharge in excellent specific capacity and cycle stability. When evaluated as a negative electrode for Sodium-ion batteries (SIBs), it exhibits excellent specific capacity (554.3 mAh g^{-1} at 0.2 A g^{-1}, first-cycle coulombic efficiency of 92.3 %), and excellent long-cycle stability (436.3 mAh g^{-1} at 1 A g^{-1} for 800 cycles), demonstrating the potential of NiS_2@NC as an ideal anode material for SIBs.

1. Introduction

The concept of carbon neutralization promotes the vigorous development of the new energy industry and increases the demand for secondary batteries [1–3]. Lithium-ion battery (LIBs) has become a widely used secondary battery because of their high energy density, excellent cycle performance, and no memory effect [4,5]. Due to the limited lithium resources on the earth, they could not meet the growing demand for energy storage. The replacements for LIBs are become urgently needed in recent years [6–8]. The SIBs has similar reaction mechanism and energy storage characteristics to LIBs. At the same time, the SIBs have some advantages of low cost, abundant reserves, more security, and a higher thermal runaway temperature than LIBs. So it has become a perfect candidate for the new generation of energy storage systems [9–12]. However, the large radius and relative molecular weight of sodium-ion lead to large volume expansion and low energy density in the process of battery reaction [13–15]. The above problems accelerate the pace of building suitable anode materials and performance optimization for SIBs. Transition metal oxides (TMO) and transition metal sulfides (TMS) are commonly used as anode materials for sodium-ion batteries with excellent electrochemical performance [16–18]. Compared with TMO, TMS has better cycling stability, smaller polarization, and better ionic conductivity. [19–21]. NiS_2 is a common TMS material. The theoretical capacity of SIBs reached 870 mAh g^{-1}, which is higher than other nickel sulfide members, and it has good potential in the field of energy storage [22,23].

However, NiS_2 has the disadvantages of large volume expansion and low electronic conductivity in the process of ion insertion and extraction [24]. To solve the above problems, researchers usually focus on nanostructure design to shorten the Na^+ diffusion path, increase the specific surface area of the material, and relieve volume expansion during repeated sodiumization/de-sodiumization. [25,26]. On this basis, suitable conductive coatings further improve the electrical conductivity of the material and finally increase the Na^+ diffusion rate and electrochemical performance [27,28]. Wen et al. have composited embedded porous carbon nanofibers with NiS_2 nanoparticles as anodes for SIBs, with a remarkably high-rate capacity of 500 mAh g^{-1} at 0.1 A g^{-1} and 200 mAh g^{-1} at 2 A g^{-1} [29]. Qian et al. have obtained the NiS_2/graphene composite by the L-cysteine-assisted hydrothermal method, which can maintain a reversible capacity of 800 mAh g^{-1} at a current density of 0.5 A g^{-1} for 900 cycles [22]. Element doping is also a strategy to further improve ionic conductivity, and enhance the specific capacity and rate capability through synergistic effects. Recently reported the synthesis of phosphorus-doped eggshell NiS_2/C microspheres by Li et al., when used as SIBs anode, the hybrid material exhibits excellent cycling

* Corresponding authors.
E-mail addresses: hecheng@mail.xjtu.edu.cn (C. He), Jiuranw@chd.edu.cn (J.R. Wen).

https://doi.org/10.1016/j.jallcom.2022.168379
0925-8388/

stability of 265 mAh g^{-1} at 1 A g^{-1} after 1000 cycles [30,31]. Therefore, the above modification strategies are worth considering.

Here, $C_4H_6O_4Ni{\cdot}4\ H_2O$ and $Na_2S_2O_3{\cdot}5\ H_2O$ are chosen as raw materials and dopamine hydrochloride as carbon source to synthesize carbon layer-coated NiS_2 nanospheres (NiS_2 @NC) by a simple PVP-assisted hydrothermal method. The amorphous carbon layer could modify the NiS_2 lattice, accelerate the intercalation and deintercalation of Na^+, help alleviate the volume expansion, and reduce the influence of side reactions. A small amount of nitrogen-doped during annealing improves the sodium ion diffusion and transfer kinetics. The stable nanosphere structure accommodates the volume effect of the cycling process and enhances the electrochemical activity of Na^+ storage. Benefiting from the above modification method, NiS_2@NC has a capacity of 554.3 mAh g^{-1} after 400 cycles at a current of 0.2 A g^{-1}, and the coulomb efficiency of the first cycle is as high as 92.3 %. After 800 cycles at a current of 1 A g^{-1}, the specific capacity is 436.3 mAh g^{-1}. NiS_2@NC has excellent electrochemical performance, making it a good choice among many SIBs anode materials.

2. Experimental section

2.1. Synthesis of NiS_2 nanospheres

0.6 g PVP-k30 was dispersed into 160 ml deionized water (DI) and 80 ml EG. Then, 2 mmol $C_4H_6O_4Ni{\cdot}4\ H_2O$ and 6 mmol $Na_2S_2O_3{\cdot}5\ H_2O$ were added to the PVP suspension in a continuous stirring process for 1 h. Next, the homogenous solution was transferred into a Teflon-lined autoclave and the autoclave was kept in an oven at 180 °C, the obtained suspension was centrifuged, and the precipitate was washed thoroughly with water and absolute ethanol. The final products were dried at 60 °C for 10 h in a vacuum oven.

2.2. Synthesis of NiS_2@NC

The obtained 0.2 g NiS_2 nanospheres and 80 mg dopamine hydrochloride were dispersed into a Tris-buffer solution (10 mM, 100 ml, pH = 8.5) under magnetic stirring at room temperature for 8 h. The black precipitates were collected by centrifugation and washing using DI water and ethanol a lot of times. The products were dried at 60 °C for 10 h, which was further annealed in Ar atmosphere at 500 °C for 2 h with a heating rate of 2 °C/min to obtain the final nitrogen-doped carbon-coated NiS_2 nanosphere, which was abbreviated as NiS_2@NC.

2.3. Materials characterizations

The phase characteristics of the materials were measured by an X-ray diffractometer (XRD, D8 ADVANCE) with a diffraction angle of 2θ = 20–80°. The surface morphologies of the materials were investigated by cold field emission scanning electron microscopy (SEM, Hitachi S-4800) and high-resolution electron microscopy (TEM, Talos L120C). X-ray photoelectron spectroscopy (XPS, Thermo Fisher ESCALAB Xi^+) investigated the chemical structure and valence information of the material surface. Thermogravimetric analysis (TGA) was performed in the air on a Shimadzu-50 thermal analyzer. The specific surface area and pore size distribution were determined by BruauerEmmett-Teller (BET) by N_2 adsorption and desorption test (Autosorb-iQ-Cx) at 77 K.

2.4. Electrochemical measurements

The active material, acetylene black and polyvinylidene fluoride (PVDF) were dissolved in NMP at a mass ratio of 8:1:1 and stirred for 12 h to prepare a working electrode. The resulting slurry was then coated on copper foil and vacuum dried for 12 h. As drafted, the working electrode was cut into 12 mm diameter disks. The counter electrode was sodium foil, the separator was glass fiber membrane, and the electrolyte was 1 M $NaClO_4$ dissolved in ethylene glycol dimethyl ether (DME). Electrochemical performance tests were carried out using a battery tester (Netware, Shenzhen) and an electrochemical workstation (CHI 600E, Shanghai Chenhua). All tests are performed at room temperature.

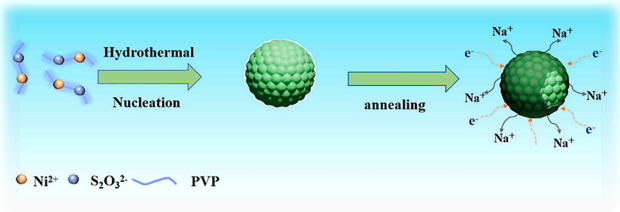

Fig. 1. Schematic illustration of the synthesis procedure of NiS_2@NC.

3. Results and discussion

Fig. 1 is a diagram of the process preparation of NiS_2@NC. Surfactant PVP can promote the surface growth of nanospheres [32]. First, Ni^{2+} and $S_2O_3^{2-}$ generated by $C_4H_6O_4Ni{\cdot}4\ H_2O$ and $Na_2S_2O_3{\cdot}5\ H_2O$ grow with the surface of the PVP. The NiS_2 nanospheres could be obtained by hydrothermal process. Then the NiS_2 were coated with polydopamine to form NiS_2@PDA through immersion into a dopamine aqueous solution. NiS_2@PDA precursor was annealed in Ar to obtain carbon-coated nitrogen-doped NiS_2 nanospheres (NiS_2@NC).

Fig. 2a-b shows that SEM images of NiS_2 and NiS_2@NC exhibited a uniform morphology of nanospheres, with the size of microspheres being about 70 nm. The surface growth of NiS_2 is accelerated and nucleation becomes uniform nanospheres due to the incorporation of PVP. From Fig. 2a, the structure of NiS_2 nanospheres did not change after dopamine hydrochloride and subsequent high-temperature annealing. Simultaneously, the N-doped carbon coating via the annealing process was formed around the microspheres. TEM and HRTEM further indicated the morphology and crystal structure of NiS_2@NC. The morphological features are similar to SEM and could be exactly seen from the low magnification TEM image (Fig. 2c), the size of the microspheres is identical, about 70 nm, and the NiS_2 @NC covering the carbon layer can be seen. The carbon layer thickness was observed to be about 2 nm by HRTEM (Fig. 2d), and the lattice fringes of NiS_2 were observed to show a lattice spacing of 0.201 nm, which matched the (220) plane of NiS_2. The above results fully prove that NiS_2 is successfully coated by the carbon layer after PDA annealing.

Fig. 3a shows the X-ray diffraction pattern of NiS_2@NC for an intuitive understanding of its crystal structure. It can be observed from the X-ray diffraction spectrum that the diffraction peaks in the figure match the standard card NiS_2 (JCPDF#80–0375). There are obvious apparent peaks at 31.6°, 35.3°, 38.8°, 45.3°, and 53.6°, corresponding to (200), (210), (211), (220), (311), respectively. The sharp diffraction peak indicates that the product has good crystallinity. There is no obvious peak related to carbon in the diffraction pattern, meaning that the carbon layer formed by PDA coating is in an amorphous form [33]. The carbon content in NiS_2@NC was determined by TGA analysis. As shown in Fig. 3b, the temperature range was set at 50–800 °C, and the calcination was carried out in an air atmosphere. The slight weight loss before 400 °C is due to the loss of adsorbed water in the composite, and the significant weight loss at 400–750 °C is due to the combustion of C and NiS_2. Based on the factual analysis, NiO (52.3 wt%) was finally retained. By calculation,

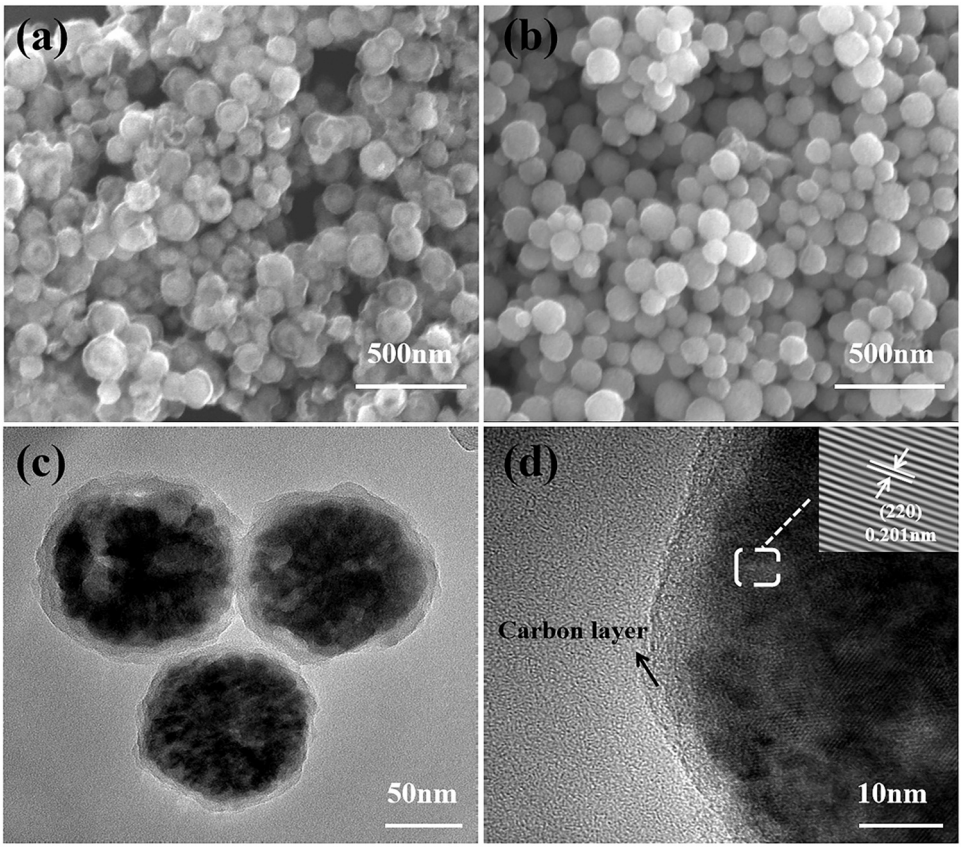

Fig. 2. Structural and morphological characterization: (a) SEM of NiS_2, (b) SEM of NiS2@NC, (c) TEM of NiS_2@NC, and (d) HRTEM image of NiS2@NC.

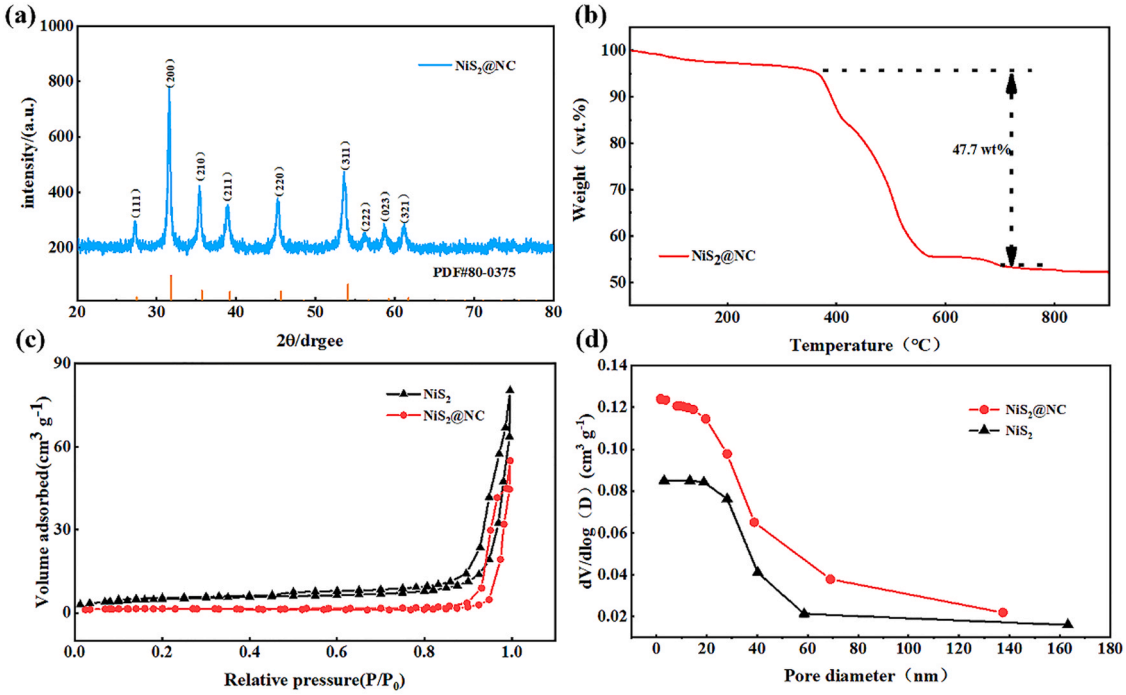

Fig. 3. XRD patterns of NiS_2@NC. (b)TGA analysis of NiS_2@NC. (c) N_2 adsorption and desorption isotherms and (d) pore size distributions of the NiS_2 and NiS_2@NC materials.

the content of NiS_2 is about 78.51 %, and the content of NC is 21.49 %. The calculation process is shown in S1.

Fig. 3c-d show the N_2 adsorption-desorption isotherms and pore size distributions of NiS_2 and NiS_2@NC, and the samples exhibit typical hysteresis loops at high pressure, indicating the existence of mesoporous distribution [34]. The BET surface area (16.3403 m^2/g) and pore volume (0.073425 cm^3/g) of NiS_2@NC are larger than those of NiS_2 (4.2912 m^2/g, 0.049516 cm^3/g). It can be seen from the pore

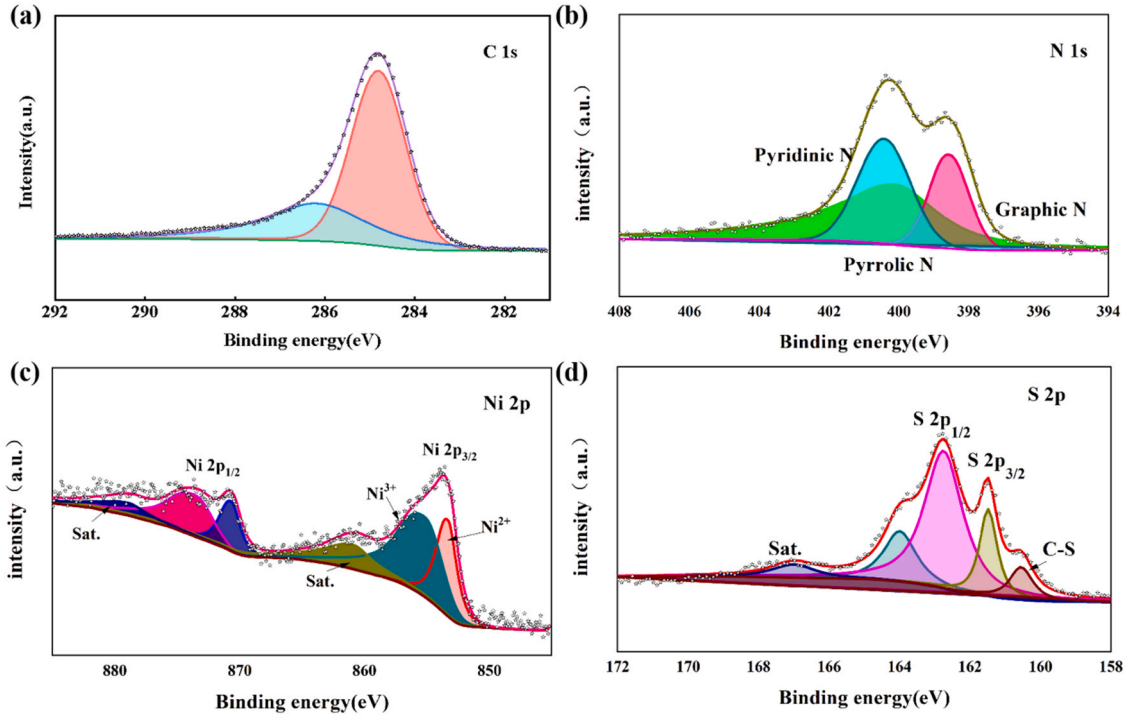

Fig. 4. (a–d) High-resolution XPS spectra of C 1s, and N 1s, Ni 2p, S 2p, of the NiS_2@NC composite material.

size distribution diagram (Fig. 3d). The pore size of the material is mostly 2–20 nm. The larger specific surface area and certain mesoporous properties of NiS_2@NC increase the contact area between the active material and the electrolyte and improve the Na^+ diffusion rate [35].

The element valence state and chemical distribution of NiS_2 @NC were characterized by X-ray electron spectroscopy (XPS). As shown in Fig. 4a, the C1s spectrum can show two characteristic peaks at 284.8 eV and 286.2 eV, corresponding to C-C and C-N-C bonds, respectively [36]. In Fig. 4b, the fitting peaks of the N1s energy spectrum at 398.7 eV, 399.8 eV, and 400.7 eV could be obtained, which are respectively assigned to pyridine N, pyrrolic N, and graphitic N, indicating that the doping of N element in NiS_2 and the existence of N element structural stability could be increased by forming defects through affinity for C [37,38]. The binding energies of Ni $2p_{3/2}$ and $2p_{1/2}$ for the NiS_2@NC are observed at around 855 and 873 eV, respectively, along with two satellite peaks at 862.1 and 879 eV. Further deconvolution of the Ni $2p_{3/2}$ spectra yields two distinct peaks, where the peak at 853.48 eV and 855.98 eV are attributed to Ni^{2+} and Ni^{3+} in the NiS_2@NC, respectively. The appearance of Ni^{3+} is due to the surface oxidation of NiS_2 [39,40]. Fig. 4d corresponds to the XPS peak of S2p, which can be deconvolved to two binding energy peaks of 162.4 eV and 163.6 eV, corresponding to $S2p_{1/2}$ and $S2p_{3/2}$, respectively. The peak at 165 eV is the concomitant peak of $S2p_{3/2}$. This indicates the existence of NiS_2 S-S bond, and the sulfur states in NiS_2@NC include not only $S2p_{1/2}$ and $S2p_{3/2}$, but also sulfur states from C-S (160.7 eV), which is related to the carbon source. The wide satellite peak at 167 eV indicates the presence of S^{2-}. [41,42]. Thus, XPS demonstrated the successful compounding of NiS_2@NC.

The cyclic voltammetry (CV) curves of NiS_2 @NC at 0.1 mV/s for the first three cycles are shown in Fig. 5a. In the first cathodic scan, a sharp and strong peak was generated at 1.17 V, which disappeared in the following two cycles, which is due to the insertion of Na^+ into the lattice to form Na_xNiS_2 (NiS_2 +xNa^++xe^-→Na_xNiS_2), which simultaneously generates in the solid electrolyte interface (SEI), the reduction peak observed at 0.87 V corresponds to the conversion reaction process of Na_xNiS_2 to Ni and Na_2S (NaxNiS$_2$ +(4-x) Na^++(4-x) e^-→Ni+ 2Na_2S). In subsequent cycles, the reduction peaks detectable at 0.87 V and 1.43 V indicate the intercalation reaction and formation of Na_xNiS_2 during discharge. In the first scan of the anode, the oxidation peaks at 1.68 V and 2 V correspond to the conversion of Ni and Na_2S to Na_xNiS_2 and the reduction of NiS_2. We can also observe that the redox peaks of the first cycle are slightly shifted from those of the subsequent cycles, which indicates that NiS_2@NC has better electrochemical reversibility. As shown in Fig. 5b, in the first three cycles, the NiS_2 @NC galvanostatic discharge test at a current density of 0.2 A g^{-1}, The first discharge and charge capacities are 640.04 and 591.36 mAh g^{-1}, respectively, and the corresponding coulombic efficiencies are about 92.3 %. The irreversible capacity of the first cycle is due to the formation of the SEI film [23,43]. After the second cycle, the discharge capacity dropped to 555.31 mAh g^{-1}, and the charge capacity dropped to 551.46 mAh g^{-1} correspondingly. The coulombic efficiency was as high as 99%, and remained above 99 % in the subsequent cycles, indicating that the sodiumization/de-sodiumization process of NiS_2@NC has good reversibility.

To further understand the effect of carbon coating and N element doping modification on the sodiumization and de-sodiumization of NiS_2@NC, further electrochemical tests have been conducted. Fig. 5c shows the cycling performance of NiS_2@NC at a current density of 0.2 A g^{-1}, and the composite exhibits excellent cycling stability compared to pure NiS_2. NiS_2@NC maintains a reversible capacity of 554.3 mAh g^{-1} after 400 cycles, significantly higher than that of NiS_2 (341.1 mAh g^{-1}). The discharge capacity of NiS_2@NC decays rapidly within the initial cycle, dropping from 640 to 489.7 mAh g^{-1} after 20 cycles, and levels off after 75 cycles, finally reaching 554.3 mAh g^{-1}. The initial decay is mainly due to the suboptimal activation process. The subsequent gradual recovery of capacity is attributed to the activation of the microspheres during cycling, which improves the electronic conductivity and accelerates the electron transfer [44–46]. Still, the capacity difference is large, which is attributed to the

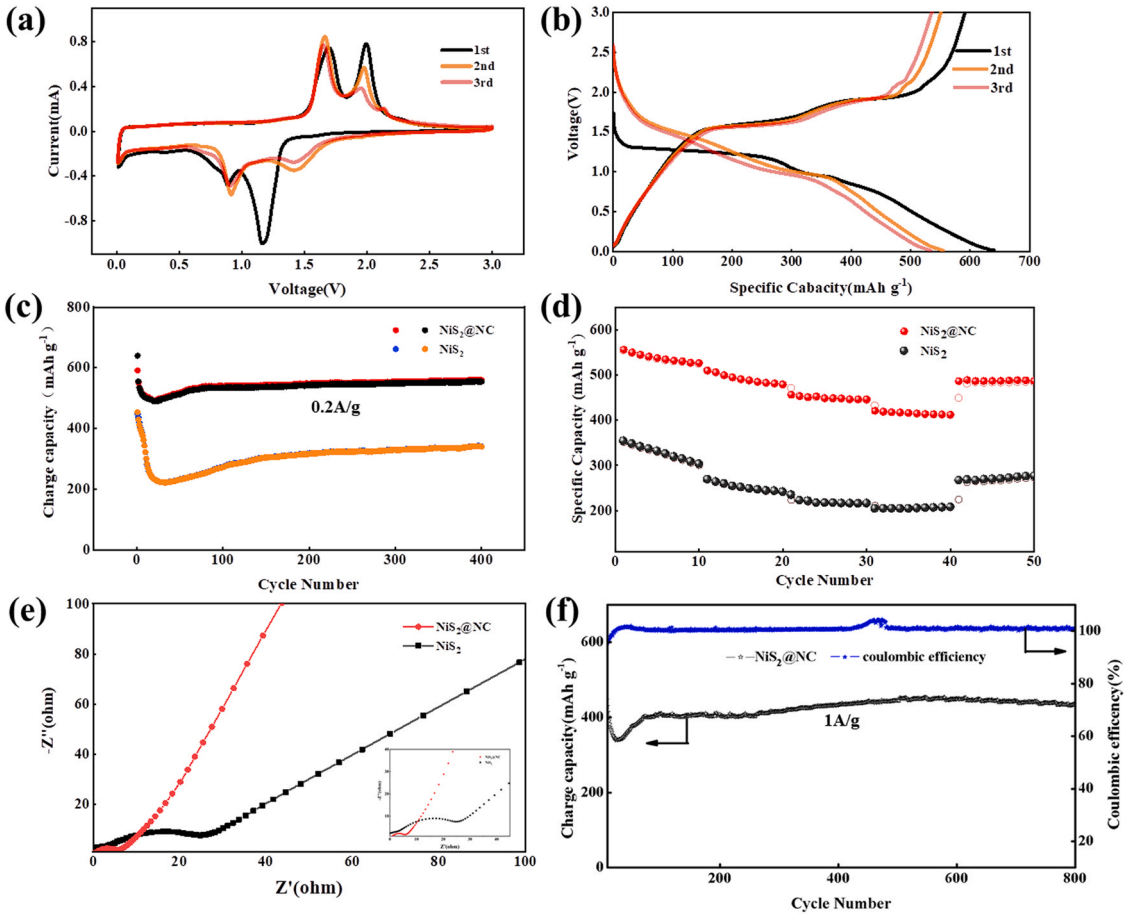

Fig. 5. (a) CV curves at 0.2 mV/s and (b) galvanostatic discharge/charge profiles for NiS_2@NC in SIBs at 0.2 A g^{-1} for the first three cycles. (c) Cycling performance at 0.2 A g^{-1} and (d) rate performance at 0.2–2 A g^{-1} of NiS_2 and NiS_2@NC. (e) Nyquist plots of NiS_2 and NiS_2@NC. (e) Cycle performance at 1 A g^{-1} of NiS_2@NC.

addition of the N element to accelerate the intercalation and deintercalation of Na^+, coating of the carbon layer improves the ionic conductivity. While releasing the structural stress, the structure is more stable. On behalf of evaluating the rate performance of the two materials, the current densities of 0.2, 0.5, 1, 2, and 0.2 A g^{-1} were set for test comparison (Fig. 5d). The capacities of NiS_2 @NC at different current densities are 524.3, 479.1, 444.7, 411.1 mAh g^{-1}. When the current returned to 0.1 A g^{-1}, the capacity remained at 483.9 mAh g^{-1}. In sharp contrast to the rate performance of NiS_2, the capacity dropped significantly. The discharge capacities were 303.7, 235.1, 216.7, 208.1, and 276 mAh g^{-1}. The differences in NiS_2 and NiS_2@NC electrochemical reaction kinetics, and electronic conductivity were further explored by EIS. As shown in Fig. 5e, the material impedance curve consists of a semicircle and an oblique line. The diameter of the arc in the high and middle-frequency region represents the charge transfer impedance (Rct), the oblique line is caused by the Warburg impedance (diffusion impedance), and its slope represents the diffusion impedance. The electrochemical process is dominated by charge transfer and Na^+ diffusion [47]. the Rct value of NiS_2@NC is smaller than that of NiS_2, and further, through the slope, it can be obtained that the Na^+ intercalation and deintercalation rate in NiS_2 @ NC is faster, and more ideal Na^+ storage is obtained dynamics. At the same time, the cycling performance of NiS_2@NC at 1 A g^{-1} (Fig. 5f) is also tested. After 800 cycles, NiS_2@NC maintained a reversible capacity of 436.3 mAh g^{-1}, and the coulombic efficiency remained above 99 %, showing its excellent long-cycle stability. Based on the above electrochemical performance analysis, the superb rate of performance of NiS_2@NC is due to the comprehensive synergistic effect of carbon layer coating and N element doping.

To further study the electrochemical reaction kinetics of NiS_2@ NC, the CV curves at different scan rates of 0.2–1.6 mV/s are analyzed (Fig. 6a). The redox peaks at different scan rates are similar in shape. When the scan rate increases, the peak current increases correspondingly, and the peak position shifts slightly, which is caused by electrode polarization [48]. The relationship between the current (i) of the CV curve and the scan rate can be obtained by the following equation to judge the capacitive effect [49]:

$$i = av^b \tag{1}$$

The b value can be estimated from the fitted line from log *v* and log *i*. The *b* value is close to 1, indicating that pseudocapacitive Na ion storage dominates the NiS_2@NC electrode, and b is close to 0.5, indicating that diffusion dominates. Fig. 6b shows the cathodic and anodic process b values of 0.711, and 0.504, which illustrate that the electrochemical reaction of NiS_2@NC is controlled by both capacitance and diffusion. We can further quantify the diffusion effect and the capacitive contribution by Eq. 2 [50]:

$$i(v) = k_1 v + k_2 v^{1/2} \tag{2}$$

Fig. 6c shows that at 0.6 mV/s the capacitive charge accounts for 80% of the total charge, and the capacitive contribution increases as the scan speed increases (Fig. 6d). Kinetic analysis shows that the capacitive process is the source of a large amount of stored charge.

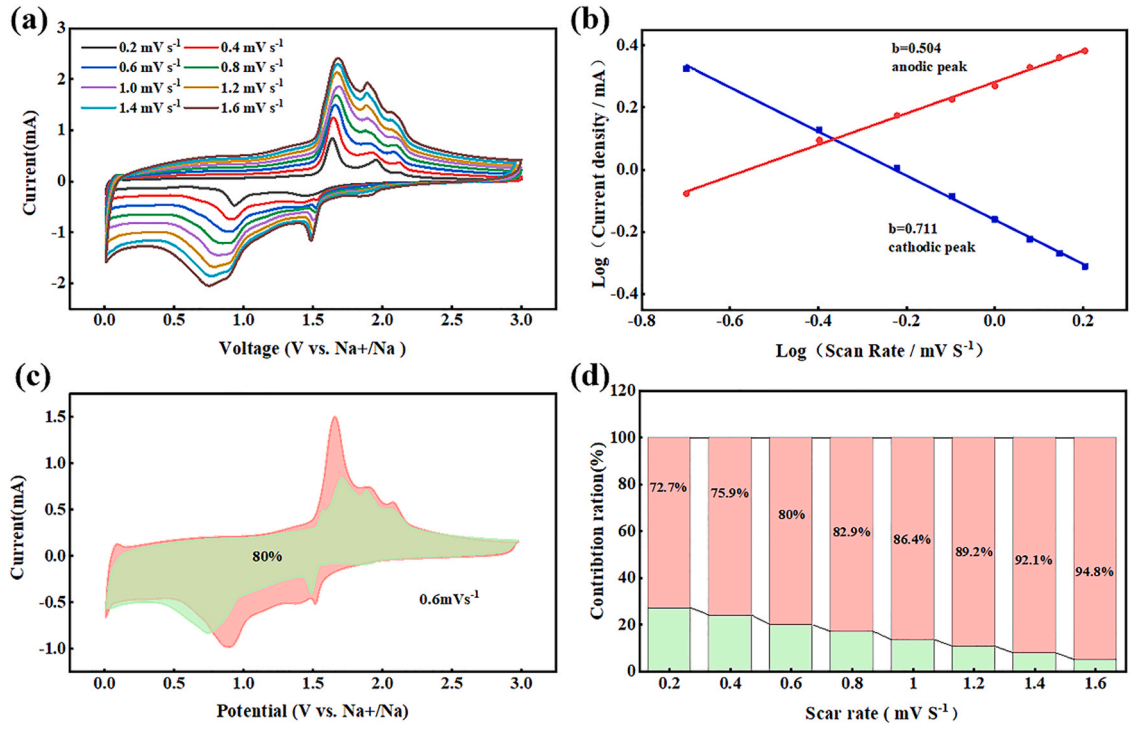

Fig. 6. (a) CV curves of NiS_2 @NC at various scan rates and (b) the corresponding log(i) vs log(v) plots. (c) Capacitive contribution of the NiS_2@NC electrode at 0.6 mV/s. (d) Contribution ratio of the capacitive and diffusive process for the NiS_2@NC electrode at different scan rates.

The carbon coating of nitrogen-doped NiS_2 nanospheres enables a faster ion transfer rate.

4. Conclusion

In summary, NiS_2@NC composites were synthesized by a simple PVP-assisted hydrothermal and subsequent annealing process. It can be seen by SEM and TEM that the NiS_2 nanospheres were covered by a thin carbon layer. The nanosphere structure reduced the volume expansion while shortening the Na^+ diffusion path and improving the Na^+ storage activity. The carbon layer significantly improved the ionic conductivity of NiS_2@NC and accelerates ion diffusion, reducing capacity loss. In addition, the doping of nitrogen further enhanced the conductivity of the material and improved the ion diffusion kinetics. The synergistic effect between the nanosphere structure and the nitrogen-doped carbon layer enhanced the specific capacity and rate capability of the battery. In SIBs, it exhibited a considerable capacity of 554.3 mAh g^{-1} at 0.2 A g^{-1} after 400 cycles. The coulombic efficiency of the first cycle is as high as 92.3 %, showing excellent sodium storage performance, while at a current density of 1 A g^{-1}, it can still maintain 436.3 mAh g^{-1} for 800 cycles, showing its good cycling stability. This modification strategy and excellent electrochemical performance made NiS_2@NC promising as an ideal anode material for SIBs.

Data availability

The authors do not have permission to share data.

Declaration of Competing Interest

The authors declare that they have no known competing financial interests or personal relationships that could have appeared to influence the work reported in this paper.

Acknowledgments

The authors acknowledge supports by National Natural Science Foundation of China (NSFC, Grant No. 51471124, U1766216), Natural Science Foundation of Shaanxi Province, China (2019JM-189, 2020JM-218), Shaanxi Province House and Urban Construction Department (2017-K58), and the Fundamental Research Funds for the Central Universities (CHD300102311405), HPC platform, Xi'an Jiaotong University.

Appendix A. Supporting information

Supplementary data associated with this article can be found in the online version at doi:10.1016/j.jallcom.2022.168379.

References

[1] V.V.S.N. Murty, A. Kumar, Multi-objective energy management in microgrids with hybrid energy sources and battery energy storage systems, Prot. Control Mod. Power Syst. 5 (2020) 2 ⟨https://10.1186/s41601-019-0147-z⟩.
[2] C. Jin, J. Nai, O. Sheng, H. Yuan, W.W. Zhang, D. Tao, D. Lou, Biomass-based materials for green lithium secondary batteries, Energy Environ. Sci. 14 (2021) 1326–1379 ⟨https://10.1039/D0EE02848G⟩.
[3] Y. Hyun, J.Y. Choi, H.K. Park, C.S. Lee, Synthesis and electrochemical performance of ruthenium oxide-coated carbon nanofibers as anode materials for lithium secondary batteries, Appl. Surf. Sci. 388 (2016) 274–280, https://doi.org/10.1016/j.apsusc.2016.01.095
[4] Y.L. Ding, Z.P. Cano, A.P. Yu, J. Lu, Z.W. Chen, Automotive Li-ion batteries: current status and future perspectives, Electrochem. Energy Rev. 2 (2019) 1–28 ⟨https://10.1007/s41918-018-0022-z⟩.
[5] B. Diouf, R. Pode, Potential of lithium-ion batteries in renewable energy, Renew. Energy 76 (2015) 375–380 ⟨https://10.1016/j.renene.2014.11.058⟩.
[6] S.L. Liu, J. Huang, J. Liu, M. Lei, J. Min, S. Li, G. Liu, Porous Mo_2N nanobelts as a new anode material for sodium-ion batteries, Mater. Lett. 172 (2016) 56–59 ⟨https://10.1016/j.matlet.2016.02.121⟩.
[7] Y.S. Wang, Z.M. Feng, P.X. Cui, W. Zhu, Y. Gong, M.A. Girard, G. Lajoie, J.L. Trottier, Q.H. Zhang, L. Gu, Pillar-beam structures prevent layered cathode materials from destructive phase transitions, Nat. Commun. 12 (2021) 1–11 ⟨https://10.1038/s41467-020-20169-1⟩.
[8] L. Ren, L.T. Song, Y.C. Guo, Y. Wu, J.L. Lian, Y.N. Zhou, W.Y. Yuan, Q. Yan, Q.Q. Wang, S.N. Ma, X.R. Ye, Z.Z. Ye, J.G. Lu, Magnesium-doped $Na_2FeP_2O_7$

cathode materials for sodium-ion battery with enhanced cycling stability and rate capability, Appl. Surf. Sci. 544 (2022) 148893, https://doi.org/10.1016/j.apsusc.2020.148893
[9] P.Z. Lyu, X.J. Liu, J. Qu, J.T. Zhao, H.R. Zhong, Recent advances of thermal safety of lithium-ion battery for energy storage, Energy Storage Mater. 31 (2020) 195–220 ⟨https://10.1016/j.ensm.2020.06.042⟩.
[10] D.H. Luo, P. Han, L.D. Shi, J.T. Huang, J.L. Yu, Y.M. Lin, J.G. Du, B. Yang, C.H. Li, C.Z. Zhu, J. Xu, Biomass-derived nitrogen/oxygen co-doped hierarchical porous carbon with a large specific surface area for ultrafast and long-life sodium-ion batteries, Appl. Surf. Sci. 462 (2018) 713–719, https://doi.org/10.1016/j.apsusc.2018.08.106
[11] Y.L. Cao, The opportunities and challenges of sodium ion battery, Energy Storage Sci. Technol. 9 (2020) 757–761 ⟨https://10.19799/j.cnki.2095-4239.2020.0026⟩.
[12] H.X. Yan, M. Yang, L. Liu, J. Xia, Y.T. Yuan, J.F. Liu, Y. Zhang, S. Nie, X.Y. Wang, Synthesis of SnS/C nanofibers membrane as self-standing anode for high-performance sodium-ion batteries by a smart process, J. Alloy. Compd. 843 (2020) 155899⟨https://10.1016/j.jallcom.2020.155899⟩.
[13] M.S. Islaml, C.A.J. Fisher, Lithium and sodium battery cathode materials: computational insights into voltage, diffusion and nanostructural properties, Chem. Soc. Rev. 43 (2014) 185–204 ⟨https://10.1039/c3cs60199d⟩.
[14] Q. Zhao, Y. Lu, J. Chen, Advanced organic electrode materials for rechargeable sodium-ion batteries, Adv. Energy Mater. 7 (2017) 1601792⟨https://10.1002/aenm.201601792⟩.
[15] Z.G. Yang, Q. Pan, Z.G. Wu, W. Xiang, F.Y. Fu, Y. Wang, L. Ji, B.H. Zhong, X.P. Sun, X.D. Guo, Self-supported cobalt phosphate nanoarray with pseudocapacitive behavior: an efficient 3D anode material for sodium-ion batteries, J. Alloy. Compd. 848 (2020) 156285⟨https://10.1016/j.jallcom.2020.156285⟩.
[16] Y.Y. Zhu, P. Nie, L.F. Shen, S.Y. Dong, Q. Sheng, H.S. Li, H.F. Luo, X.G. Zhang, High rate capability and superior cycle stability of a flower-like Sb_2S_3 anode for high-capacity sodium ion batteries, Nanoscale 7 (2015) 3309–3315 ⟨https://10.1039/c4nr05242k⟩.
[17] Y. Zheng, T.F. Zhou, C.F. Zhang, J.F. Mao, H.K. Liu, Z.P. Guo, Boosted charge transfer in SnS/SnO_2 heterostructures: toward high rate capability for sodium-ion batteries, Angew. Chem. 128 (2016) 3469–3474 ⟨https://10.1002/anie.201510978⟩.
[18] M.R. Li, K.T. Zheng, J.J. Zhang, X.M. Li, C.X. Jian, Design and construction of 2D/2D sheet-on-sheet transition metal sulfide/phosphide heterostructure for efficient oxygen evolution reaction, Appl. Surf. Sci. 565 (2021) 150510, https://doi.org/10.1016/j.apsusc.2021.150510
[19] K. Rajan, T. Dheivasigamani, P. Natarajan, H. Yasuhiro, Single-step synthesis and catalytic activity of structure-controlled nickel sulfide nanoparticles, CrystEngComm 17 (2015) 5431–5439 ⟨https://10.1039/C5CE00742A⟩.
[20] M.S. Faber, M.A. Lukowski, Q. Ding, N.S. Kaiser, S. Jin, Earth-abundant metal pyrites (FeS_2, CoS_2, NiS_2, and their alloys) for highly efficient hydrogen evolution and polysulfide reduction electrocatalysis, J. Phys. Chem. C 118 (2014) 21347–21356 ⟨https://10.1021/jp506288w⟩.
[21] S.H. Guo, Y. Feng, J.H. Qiu, X.D. Li, J.F. Yao, Leaf-shaped bimetallic sulfides@ N-doped porous carbon as advanced lithium-ion battery anode, J. Alloy. Compd. 792 (2019) 8–15 ⟨https://10.1016/j.jallcom.2019.03.398⟩.
[22] Q.N. Chen, W.X. Chen, J.B. Ye, Z. Wang, J.Y. Lee, L-Cysteine-assisted hydrothermal synthesis of nickel disulfide/graphene composite with enhanced electrochemical performance for reversible lithium storage, J. Power Sources 294 (2015) 51–58 ⟨https://10.1016/j.jpowsour.2015.06.071⟩.
[23] T.S. Wang, P. Hu, C.J. Zhang, H.P. Du, Z.H. Zhang, X.G. Wang, S.G. Chen, J.W. Xiong, G.L. Cui, Nickel disulfide–graphene nanosheets composites with improved electrochemical performance for sodium-ion battery, ACS Appl. Mater. Interfaces 8 (2016) 7811–7817 ⟨https://10.1021/acsami.6b00179⟩.
[24] W.X. Zhao, X. Hu, J.X. Chen, Z.H. Wen, Highly dispersed ultrasmall NiS_2 nanoparticles in porous carbon nanofiber anodes for sodium-ion batteries, Nanoscale 11 (2019) 4688–4695 ⟨https://10.1039/c9nr00160c⟩.
[25] C.G. Hu, L.X. Lv, J.L. Xue, M.H. Ye, L.X. Wang, L.T. Qu, Branched graphene nanocapsules for anode material of lithium-ion batteries, Chem. Mater. 27 (2015) 5253–5260 ⟨https://10.1021/acs.chemmater.5b01398⟩.
[26] L. Yue, M. Jayapal, X.L. Cheng, T.T. Zhang, J.F. Chen, X.Y. Ma, X. Dai, H.Q. Lu, R.F. Guan, W.H. Zhang, Highly dispersed ultra-small nano Sn-SnSb nanoparticles anchored on N-doped graphene sheets as high performance anode for sodium ion batteries, Appl. Surf. Sci. 512 (2020) 145686, https://doi.org/10.1016/j.apsusc.2020.145686
[27] J. Bai, B.C. Zhao, X. Wang, H.Y. Ma, K.Z. Li, H. Li, J.M. Dai, X.B. Zhu, Y.P. Sun, Yarn ball-like MoS_2 nanospheres coated by nitrogen-doped carbon for enhanced lithium and sodium storage performance, J. Power Sources 465 (2020) 228282⟨https://10.1016/j.jpowsour.2020.228282⟩.
[28] M.A.U. Din, S. Irfan, S. Jamil, S.U. Dar, Q.U. Khan, M.S. Saleem, N.P. Cheng, Graphene-like ultrathin bismuth selenide nanosheets as highly stable anode material for sodium-ion battery, J. Alloy. Compd. 901 (2022) 163572⟨https://10.1016/j.jallcom.2021.163572⟩.
[29] Y. Lin, Z.Z. Qiu, D.Z. Li, S. Ullah, H. Yang, H. Xin, W. Liao, B. Yang, H. Fan, J. Xu, NiS_2@CoS_2 nanocrystals encapsulated in N-doped carbon nanocubes for high performance lithium/sodium-ion batteries, Energy Storage Mater. 11 (2017) 67–74 ⟨https://10.1016/j.ensm.2017.06.001⟩.
[30] L.Q. Wang, Z.L. Han, Q.Q. Zhao, X.Y. Yao, Y.Q. Zhu, X.L. Ma, S.D. Wu, C.B. Cao, Engineering yolk–shell P-doped NiS_2/C spheres via a MOF-template for high-performance sodium-ion batteries, J. Mater. Chem. A 8 (2020) 8612–8619 ⟨https://10.1039/D0TA02568B⟩.
[31] Y.Y. Wang, W.P. Kang, D.X. Cao, X.Y. Fan, H.B. Yang, Z.C. Yang, D.F. Sun, Yolk-shell ZnS@NC@MoS2 nanoboxes with enhanced sodium storage capability, Appl. Surf. Sci. 574 (2021) 151715, https://doi.org/10.1016/j.apsusc.2021.151715
[32] K.M. Koczkur, S. Mourdikoudis, L. Polavarapu, S.E. Skrabalak, Polyvinylpyrrolidone (PVP) in nanoparticle synthesis, Dalton Trans. 44 (2015) 17883–17905 ⟨https://10.1039/C5DT02964C⟩.
[33] D.L. Zhang, H.Y. Mou, L. Chen, G. Xing, D.B. Wang, C.X. Song, Surface/interface engineering N-doped carbon/NiS_2 nanosheets for efficient electrocatalytic H_2O splitting, Nanoscale 12 (2020) 3370–3376 ⟨https://10.1039/C9NR10173J⟩.
[34] J.B. Li, D. Yan, X.J. Zhang, S.J. Hou, T. Lu, Y. Yao, L. Pan, ZnS nanoparticles decorated on nitrogen-doped porous carbon polyhedra: a promising anode material for lithium-ion and sodium-ion batteries, J. Mater. Chem. A 5 (2017) 20428–20438 ⟨https://10.1039/C7TA06180C⟩.
[35] J.H. Lu, F. Lian, L.L. Guang, Y.X. Zhang, F. Ding, Adapting FeS_2 micron particles as an electrode material for lithium-ion batteries via simultaneous construction of CNT internal networks and external cages, J. Mater. Chem. A 7 (2019) 991–997 ⟨https://10.1039/C8TA09955C⟩.
[36] F. Zou, Y.M. Chen, K. Liu, Z. Yu, W. Liang, S.M. Bhaway, M. Gao, Y. Zhu, Metal organic frameworks derived hierarchical hollow NiO/Ni/graphene composites for lithium and sodium storage, ACS Nano 1 (2016) 377–386 ⟨https://10.1021/acsnano.5b05041⟩.
[37] X. Xu, R.S. Zhao, W. Ai, B. Chen, H.F. Du, L.S. Wu, H. Zhang, W. Huang, T. Yu, Controllable design of MoS_2 nanosheets anchored on nitrogen-doped graphene: toward fast sodium storage by tunable pseudocapacitance, Adv. Mater. 30 (2018) 1800658⟨https://10.1002/adma.201800658⟩.
[38] J.L. Zhu, Y.Y. Li, S. Kang, X.L. Wei, P.K. Shen, One-step synthesis of Ni_3S_2 nanoparticles wrapped with in situ generated nitrogen-self-doped graphene sheets with highly improved electrochemical properties in Li-ion batteries, J. Mater. Chem. A 2 (2014) 3142–3147 ⟨https://10.1039/C3TA14562J⟩.
[39] T. Tian, L. Huang, L.H. Ai, J. Jiang, Surface anion-rich NiS_2 hollow microspheres derived from metal-organic frameworks as a robust electrocatalyst for hydrogen evolution reaction, J. Mater. Chem. A 39 (2017) 20985–20992, https://doi.org/10.1039/C7TA06671F
[40] Y.M. Lin, Z.Z. Qiu, D.Z. Li, S. Ullaha, H. Yang, H.L. Xin, W.D. Liao, B. Yang, H.S. Fan, J. Xu, C.Z. Zhu, NiS_2@CoS_2 nanocrystals encapsulated N-doped carbon nanocubes for high-performance lithium/sodium ion batteries, Energy Storage Mater. 11 (2018) 2405–8297, https://doi.org/10.1016/j.ensm.2017.06.001
[41] X. Zhang, K. Liu, S. Zhang, F. Miao, G. Shao, Enabling remarkable cycling performance of high-loading MoS_2@Graphene anode for sodium ion batteries with tunable cut-off voltage, J. Power Sources 458 (2020) 228040, https://doi.org/10.1016/j.jpowsour.2020.228040
[42] J. Yin, Y.X. Li, F. Lv, M. Lu, K. Sun, W. Wang, L. Wang, F.Y. Cheng, Y.F. Li, P.X. Xi, S.J. Guo, Oxygen vacancies dominated NiS_2/CoS_2 interface porous nanowires for portable Zn–air batteries driven water splitting devices, Adv. Mater. 29 (2017) 0935–9648, https://doi.org/10.1002/adma.201704681
[43] R. Liu, W. Cao, D. Han, Y. Mo, H. Zeng, H. Yang, W. Li, Nitrogen-doped Nb_2CTx MXene as anode materials for lithium-ion batteries, J. Alloy. Compd. 793 (2019) 505–511 ⟨https://10.1016/j.jallcom.2019.03.209⟩.
[44] R. Wu, D.P. Wang, X. Rui, B. Liu, K. Zhou, A.W. Law, Q. Yan, J. Wei, Z. Chen, In-situ formation of hollow hybrids composed of cobalt sulfides embedded within porous carbon polyhedra/carbon nanotubes for high-performance lithium-ion batteries, Adv. Mater. 27 (2015) 3038–3044 ⟨https://10.1002/adma.201500783⟩.
[45] X.S. Wang, D. Chen, Z.H. Yang, X.H. Zhang, C. Wang, J.T. Chen, X.X. Zhang, M.Q. Xue, Novel metal chalcogenide SnSSe as a high-capacity anode for sodium-ion batteries, Adv. Mater. 28 (2016) 8645–8650 ⟨https://10.1002/adma.201603219⟩.
[46] X.S. Song, X.F. Li, Z.M. Bai, B. Yan, D.J. Li, X.L. Sun, Morphology-dependent performance of nanostructured Ni_3S_2/Ni anode electrodes for high performance sodium-ion batteries, Nano Energy 26 (2016) 533–540 ⟨https://10.1016/j.nanoen.2016.06.019⟩.
[47] Y.Y. Chen, X.D. Hu, B. Evanko, H.X. Sun, X. Li, Y.T. Hou, S. Cai, C.M. Zheng, W.B. Hu, G.D. Stucky, High-rate FeS_2/CNT neural network nanostructure composite anodes for stable, high-capacity sodium-ion batteries, Nano Energy 46 (2018) 117–127 ⟨https://j.nanoen.2018.01.039⟩.
[48] L.Q. Wang, Q.Q. Zhao, Z.T. Wang, Y.J. Wu, X.L. Ma, Y.Q. Zhu, C.B. Cao, Cobalt-doping SnS_2 nanosheets towards high-performance anodes for sodium-ion batteries, Nanoscale 12 (2020) 248–255 ⟨https://10.1039/C9NR07849E⟩.
[49] V. Augustyn, J. Come, A.L. Michael, J.W. Kim, P.L. Taberna, S.H. Tolbert, H.D. Abruna, P. Simon, B. Dunn, High-rate electrochemical energy storage through Li^+ intercalation pseudocapacitance, Nat. Mater. 12 (2013) 518–522 ⟨https://10.1038/nmat3601⟩.
[50] M. Yu, L.Y. Sun, X.H. Ning, Controllable synthesis of carbon-coated Fe_3O_4 nanorings with high Li^+/Na^+ storage performance, J. Alloy. Compd. 878 (2021) 160359⟨https://10.1016/j.jallcom.2021.160359⟩.